nature medicine

Functionally defined therapeutic targets in diffuse intrinsic pontine glioma

Catherine S Grasso[1,24], Yujie Tang[2–5,23,24], Nathalene Truffaux[6,24], Noah E Berlow[7], Lining Liu[2–5], Marie-Anne Debily[6,8], Michael J Quist[1], Lara E Davis[9], Elaine C Huang[9], Pamelyn J Woo[2–5], Anitha Ponnuswami[2–5], Spenser Chen[2–5], Tessa B Johung[2–5], Wenchao Sun[2], Mari Kogiso[10], Yuchen Du[10], Lin Qi[10], Yulun Huang[10,23], Marianne Hütt-Cabezas[11,12], Katherine E Warren[13], Ludivine Le Dret[6], Paul S Meltzer[13], Hua Mao[10], Martha Quezado[13], Dannis G van Vuurden[14,15], Jinu Abraham[9], Maryam Fouladi[16], Matthew N Svalina[1,17], Nicholas Wang[1], Cynthia Hawkins[18,19], Javad Nazarian[20], Marta M Alonso[21], Eric H Raabe[11,12], Esther Hulleman[14,15], Paul T Spellman[1], Xiao-Nan Li[10], Charles Keller[9,17,25], Ranadip Pal[7,25], Jacques Grill[6,22,25] & Michelle Monje[2–5,25]

© 2015 Nature America, Inc. All rights reserved.

Diffuse intrinsic pontine glioma (DIPG) is a fatal childhood cancer. We performed a chemical screen in patient-derived DIPG cultures along with RNA-seq analyses and integrated computational modeling to identify potentially effective therapeutic strategies. The multi–histone deacetylase inhibitor panobinostat demonstrated therapeutic efficacy both *in vitro* and in DIPG orthotopic xenograft models. Combination testing of panobinostat and the histone demethylase inhibitor GSK-J4 revealed that the two had synergistic effects. Together, these data suggest a promising therapeutic strategy for DIPG.

DIPG is the leading cause of pediatric death by brain tumor. Median survival after diagnosis is only 9 months, and 5-year survival is less than 1% (ref. 1). Historically, DIPG research has been limited by a dearth of tumor tissue available for study and a lack of experimental model systems. Recently, both cell cultures derived from patients with DIPG and orthotopic xenograft models have been established[2,3]. Genomic studies of DIPG tumor tissue identified recurrent K27M mutations in genes encoding histone H3 (refs. 4–6), resulting in inhibition of the polycomb repressive complex 2 (PCR2) methyltransferase and global hypomethylation of histone H3 Lys27 (H3K27)[7,8]. Armed with these important insights and new tools, we formed an international collaboration to pool DIPG tissue resources and evaluate functional targets for DIPG therapy.

We assembled a panel of 14 patient-derived DIPG cell cultures, created using neurosphere and adherent models and obtained from both biopsy and autopsy samples[9–11] (**Fig. 1a**), representing the breadth of DIPG cell cultures available worldwide at the initiation of the study. Two additional cell cultures[3] were subsequently added (**Fig. 1**). Clinical, histopathological, and molecular characteristics of the cultures are summarized in **Supplementary Tables 1** and **2**. We performed whole-exome sequencing (WES) of the culture models used for drug screening when primary tumor DNA was available (WES data for 7/9 tumors not previously reported[10] are described here); additional DIPG tumors not associated with cultures ($n = 15$) were also sequenced to add to the publicly available DIPG genomic data ($n = 22$ DIPG tumors with WES data; **Supplementary Fig. 1** and **Supplementary Table 3**).

Using this DIPG culture panel, we screened 83 drugs selected by pediatric neurooncologists as either promising targeted agents for cancer or traditional chemotherapeutic agents in use for pediatric brain tumor therapy. Readout was cell viability at 72 h. We found sensitivity to a limited number of drugs (14/83 compounds demonstrated activity against three or more DIPG cultures; **Fig. 1a** and **Supplementary Fig. 2**). The chemical screen and subsequent validation experiments revealed DIPG cell sensitivity to histone deacetylase (HDAC) inhibitors, as well to as a limited number of other agents (**Fig. 1a–c** and **Supplementary Fig. 2**). Notable 'misses' that highlight the resistance of this tumor to traditional chemotherapies included carboplatin and vincristine (**Fig. 1a**).

To examine the molecular context of functional drug screening results, RNA deep sequencing (RNA-seq) was performed to analyze gene expression in primary DIPG tumors versus healthy, paired cerebral cortex tissue (**Supplementary Fig. 3**). Screening and RNA-seq data

[1]Center for Spatial Systems Biomedicine, Department of Molecular and Medical Genetics, Oregon Health & Science University (OHSU), Portland, Oregon, USA. [2]Department of Neurology, Stanford University, Stanford, California, USA. [3]Department of Neurosurgery, Stanford University, Stanford, California, USA. [4]Department of Pediatrics, Stanford University, Stanford, California, USA. [5]Department of Pathology, Stanford University, Stanford, California, USA. [6]CNRS, UMR 8203, Gustave Roussy, Université Paris-Sud, Villejuif, France. [7]Electrical and Computer Engineering, Texas Tech University, Lubbock, Texas, USA. [8]Département de biologie, Université d'Evry-Val d'Essone, Evry, France. [9]Pediatric Cancer Biology Program, Papé Family Pediatric Research Institute, Department of Pediatrics, OHSU, Portland, Oregon, USA. [10]Laboratory of Molecular Neurooncology, Texas Children's Cancer Center, Baylor College of Medicine, Houston, Texas, USA. [11]Department of Oncology, Johns Hopkins University, Baltimore, Maryland, USA. [12]Department of Pathology, Johns Hopkins University, Baltimore, Maryland, USA. [13]National Cancer Institute, Bethesda, Maryland, USA. [14]Department of Pediatric Oncology and Hematology, VU University Medical Center, Amsterdam, The Netherlands. [15]Neuro-Oncology Research Group Cancer Center Amsterdam, VU University Medical Center, Amsterdam, The Netherlands. [16]Cancer and Blood Diseases Institute, Cincinnati Children's Hospital Medical Center, Cincinnati, Ohio, USA. [17]Children's Cancer Therapy Development Institute, Fort Collins, Colorado, USA. [18]Department of Pediatric Laboratory Medicine, University of Toronto, Toronto, Ontario, Canada. [19]Labatt Brain Tumor Research Centre, Hospital for Sick Children, University of Toronto, Toronto, Ontario, Canada. [20]Center for Research Institute, Children's National Health Systems, Washington, DC, USA. [21]Department of Oncology, University Hospital of Navarra, Pamplona, Spain. [22]Departement de Cancerologie de l'Enfant et de l'Adolescent, Institut Gustave Roussy, Université Paris-Sud, Villejuif, France. [23]Present addresses: Key Laboratory of Cell Differentiation and Apoptosis of National Ministry of Education, Department of Pathophysiology, Shanghai Jiao Tong University School of Medicine, Shanghai, China (Y.T.) and Department of Neurosurgery, The First Affiliated Hospital of Suzhou University, Suzhou, China (Y.H.). [24]These authors contributed equally to this work. [25]These authors jointly directed this work. Correspondence should be addressed to M.M. (mmonje@stanford.edu) or C.K. (charles@cc-TDI.org).

Received 9 December 2014; accepted 10 April 2015; published online 4 May 2015; doi:10.1038/nm.3855

were then used in an integrative predictive modeling approach to determine tumor drug sensitivity using target inhibitor maps (TIMs)[12,13]; the DIPG TIM predictions and *in vitro* validations are presented in **Supplementary Figs. 3** and **4** and **Supplementary Table 4**.

We selected the multi-HDAC inhibitor panobinostat[14], which was among the most effective agents in the screen (**Fig. 1** and **Supplementary Fig. 2**), for further exploration. In total, 12/16 DIPG cultures demonstrated sensitivity to panobinostat (**Fig. 1**). Compared to vorinostat, panobinostat illustrated substantially greater potency against DIPG cells (**Fig. 1b** and **Supplementary Fig. 5**). Testing cell viability at 24, 48 and 72 h at various dose levels of panobinostat demonstrated decreased viability by 48 h (**Fig. 1c**). Expression of proliferation-associated genes *MKI67* and *CCND1* in DIPG cells decreased with time after panobinostat exposure (**Supplementary Fig. 6a**). FACS analysis of 5-ethynyl-2′-deoxyuridine (EdU) incorporation and annexin V staining revealed dose-dependent decreased cell proliferation and increased cell death (**Fig. 2a** and **Supplementary Fig. 6b**). Furthermore, short hairpin RNA (shRNA)-mediated

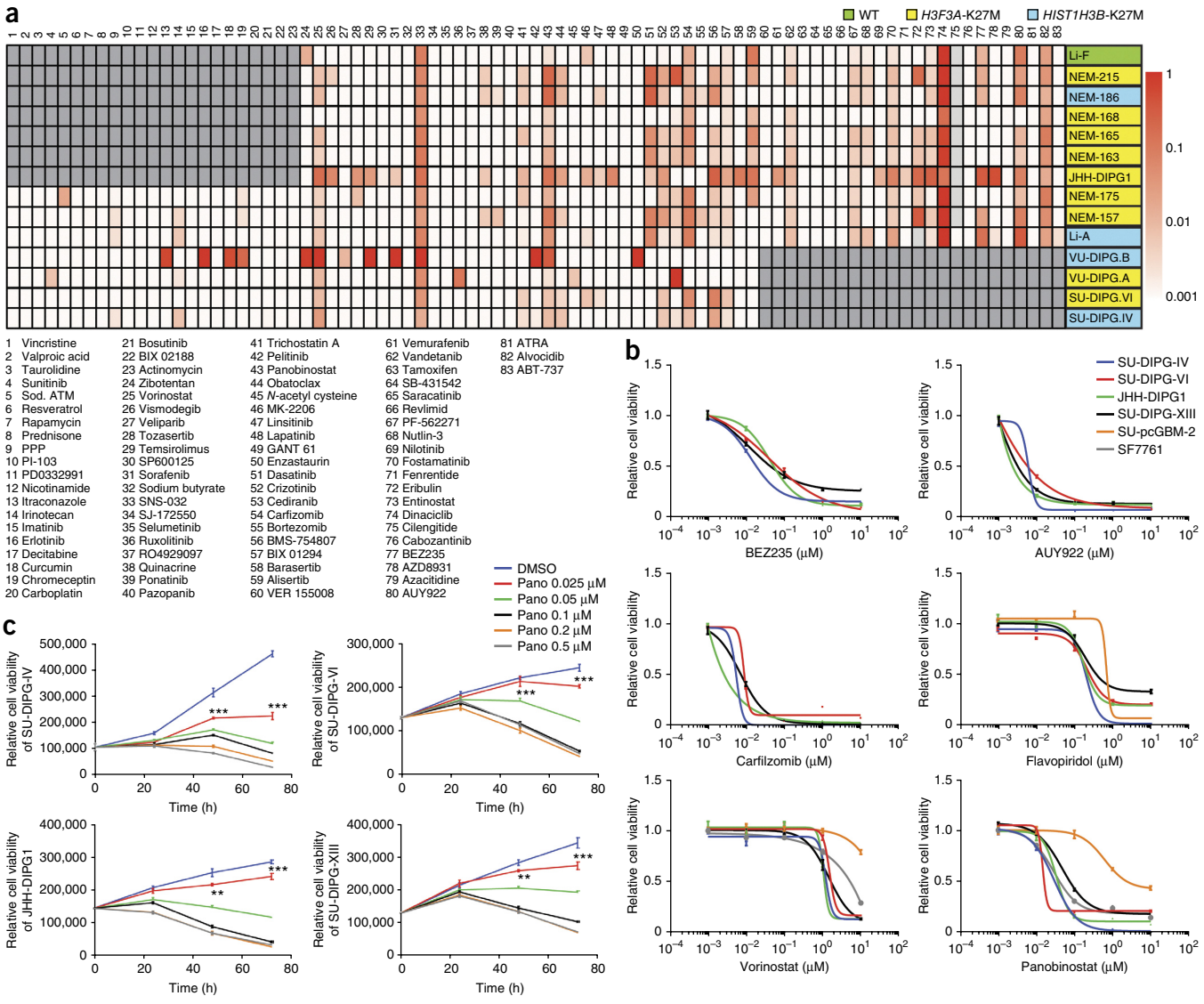

Figure 1 Functionally defined targets in DIPG therapy. (**a**) Heat map demonstrating DIPG cell line sensitivity to each of the 83 agents tested in a chemical screen of 14-patient derived DIPG cell cultures. The values shown are the absolute IC_{50} divided by the maximum dose. All drugs had a maximum dose of 10 μM except for drugs 26, 32, 40, 59 and 61, which had a maximum dose of 100 μM. Values are shown as gradations of red to white: red, submicromolar IC_{50} values; white, IC_{50} greater than the maximum dose for that drug (i.e., 10 μM or 100 μM); pink, the range in between. Gray boxes indicate drugs not included in the screen for that cell line. Numbers corresponding to the drug names in the key below the heat map are listed above, and culture IDs are listed at right. The histone status of each culture used in the screen is indicated by green (wild type, WT), yellow (H3.3K27M, *H3F3A*-K27M) or blue (H3.1K27M, *HIST1H3B*-K27M); see also **Supplementary Table 1**. Recurrent 'hits' are visible as a column of red or pink. (**b**) Dose-response curves of patient-derived DIPG lines (SU-DIPG-IV, SU-DIPG-VI, SU-DIPG-XIII, JHH-DIPG1 or SF7761 (ref. 3)) treated with the indicated drugs (*x*-axis) at 0.001, 0.01, 0.1, 1 or 10 μM or with 0.1% DMSO (vehicle control). $n = 3$ wells per condition. Cell viabilities were assessed at 72 h. Data are expressed relative to control. A pediatric cortical glioblastoma cell line (SU-pcGBM-2; histone WT) was treated in parallel for comparison in a subset. Data are shown as mean ± s.d. (**c**) Panobinostat time course: DIPG cells were treated with panobinostat at the indicated concentrations (25–500 nM) or with control. $n = 4$ wells per condition. Cell viabilities were assessed at 0, 24, 48 and 72 h after treatment. Data are shown as mean ± s.d. $^{**}P < 0.01$, $^{***}P < 0.001$; two-tailed *t*-test; results are shown for the lowest concentration that revealed a significant difference at 48 or 72 h.

© 2015 Nature America, Inc. All rights reserved.

knockdown of *HDAC1* or *HDAC2* in the DIPG cells decreased cell viability (**Fig. 2b** and **Supplementary Fig. 6c–e**). Western blot analyses of cells expressing the H3.3K27M mutation demonstrated a dose-dependent increase in H3 acetylation and H3K27 trimethylation following panobinostat treatment (**Fig. 2c**), suggesting that the drug produced partial rescue of the H3K27M-induced global hypotrimethylation phenotype. Increased K27 trimethylation was an unexpected effect of the drug, but it is consistent with recent findings that polyacetylation of the H3 N-terminal tail can 'detoxify' K27M-induced inhibition of PCR2 (ref. 15). RNA-seq performed on panobinostat- or vehicle-treated DIPG cells revealed sweeping differences in gene expression, including normalization of the K27M gene expression signature[16] and decrease of the oncogenic *MYC* target gene-expression signature in panobinostat-treated cells (**Supplementary Figs. 7** and **8**).

We next used convection-enhanced delivery (CED)[17] to directly infuse panobinostat into the pons of a DIPG orthotopic xenograft mouse model engineered to express firefly luciferase (SU-DIPG-VI-luc; H3.3K27M subtype). *In vivo* bioluminescence imaging was performed immediately before and 7 d after panobinostat (or vehicle

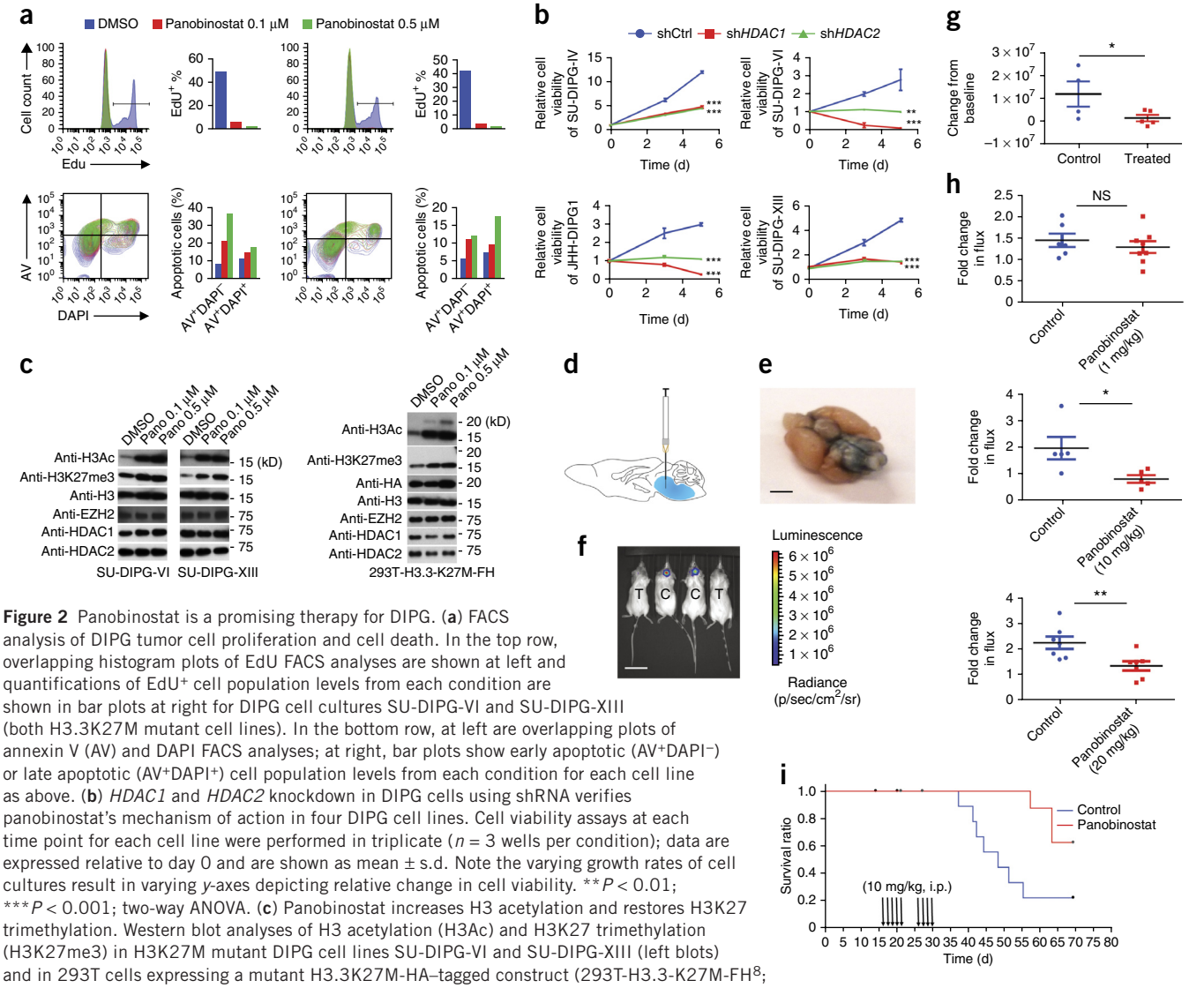

Figure 2 Panobinostat is a promising therapy for DIPG. (**a**) FACS analysis of DIPG tumor cell proliferation and cell death. In the top row, overlapping histogram plots of EdU FACS analyses are shown at left and quantifications of EdU$^+$ cell population levels from each condition are shown in bar plots at right for DIPG cell cultures SU-DIPG-VI and SU-DIPG-XIII (both H3.3K27M mutant cell lines). In the bottom row, at left are overlapping plots of annexin V (AV) and DAPI FACS analyses; at right, bar plots show early apoptotic (AV$^+$DAPI$^-$) or late apoptotic (AV$^+$DAPI$^+$) cell population levels from each condition for each cell line as above. (**b**) *HDAC1* and *HDAC2* knockdown in DIPG cells using shRNA verifies panobinostat's mechanism of action in four DIPG cell lines. Cell viability assays at each time point for each cell line were performed in triplicate ($n = 3$ wells per condition); data are expressed relative to day 0 and are shown as mean ± s.d. Note the varying growth rates of cell cultures result in varying *y*-axes depicting relative change in cell viability. $^{**}P < 0.01$; $^{***}P < 0.001$; two-way ANOVA. (**c**) Panobinostat increases H3 acetylation and restores H3K27 trimethylation. Western blot analyses of H3 acetylation (H3Ac) and H3K27 trimethylation (H3K27me3) in H3K27M mutant DIPG cell lines SU-DIPG-VI and SU-DIPG-XIII (left blots) and in 293T cells expressing a mutant H3.3K27M-HA–tagged construct (293T-H3.3-K27M-FH[8]; right blots). Controls included total protein levels of H3, HDAC1, HDAC2 and EZH2. Expression of the HA (hemagglutinin) tag in the 293T cells confirms expression of the H3.3K27M-FH construct. (**d**) Schematic illustrating convection-enhanced delivery strategy to infuse drug into brainstem. Blue, approximate distribution of the infused solution. (**e**) Distribution of infusate illustrated by delivering blue dye to the brainstem by CED. Ventral side of a mouse brain is shown immediately following CED delivery of Coomassie Blue dye. Scale bar, 3 mm. (**f**) *In vivo* bioluminescence imaging of DIPG xenografts 7 d following CED delivery of panobinostat (T) or vehicle (DMSO) control (C). The heat map superimposed over the mouse heads represents the degree of photon emission by DIPG cells expressing firefly luciferase. Scale bar, 3.5 cm. (**g**) *In vivo* DIPG xenograft tumor growth as measured by change in bioluminescent photon emission over the 7 d following CED delivery of panobinostat. $n = 5$ panobinostat-treated mice, 4 control mice. Data points represent the change in maximum photon flux between day 0 and day 7 for each mouse. (**h**) As in **g**, but with systemic administration of panobinostat. Three systemic dose levels were used: 1 mg/kg ($n = 6$ control, 8 treated mice) or 10 mg/kg ($n = 5$ mice per group) delivered i.p. three times per week or 20 mg/kg ($n = 7$ mice per group) delivered once per week. Data expressed as fold change in photon flux compared to baseline. Error bars, mean ± s.e.m. $^{*}P < 0.\ 0.5$, $^{**}P < 0.01$; NS, not significant; two-tailed *t*-test. (**i**) Systemic delivery of panobinostat prolongs survival in an H3 wild-type DIPG orthotopic xenograft model IBs-W0128DIPG. Black dots, overlapping red and blue survival curves at early time points; arrows, administration of 10 mg/kg panobinostat i.p. $n = 10$ per group; $P = 0.0179$; log-rank analysis.

© 2015 Nature America, Inc. All rights reserved.

control) administration to assess tumor growth (**Fig. 2d–g**). We confirmed that panobinostat does not downregulate the luciferase transgene (**Supplementary Fig. 9a**). We observed a marked effect of panobinostat on the rate of DIPG xenograft growth: vehicle-treated control mice exhibited xenograft growth ~6.5-fold greater than mice treated with a single dose of panobinostat by CED (n = 4 vehicle controls, 5 treated mice; $P < 0.05$ by two-tailed t-test; **Fig. 2g** and **Supplementary Fig. 9b**). We next investigated pontine penetration of panobinostat following systemic administration using liquid chromatography/tandem mass spectrometry (LC-MS/MS). Following a single 20 mg/kg intraperitoneal (i.p.) dose, pontine panobinostat levels were 0.068 ng/mg, or ~200 nM (**Supplementary Table 5**). We found that the DIPG IC_{50} for panobinostat was ~100 nM (**Fig. 1c**), so we reasoned that systemic delivery of the drug may prove effective for treating DIPG. Mice with SU-DIPG-VI-luc orthotopic xenografts were treated with 1, 10 or 20 mg/kg i.p. panobinostat-dosed three times/week (1 and 10 mg/kg groups) or once per week (20 mg/kg group) for 4 weeks. At 1 week, we observed a significant reduction in the tumor growth of animals treated with either 10 mg/kg or 20 mg/kg panobinostat, as compared to vehicle-treated controls (n = 5 per group and 7 per group; $P < 0.05$ and 0.01 by two-tailed t-test in 10 and 20 mg/kg groups, respectively; **Fig. 2h**). At 4 weeks, tumor growth was reduced only in the 20 mg/kg panobinostat–treated group (**Supplementary Fig. 9c**). We tested a second patient-derived DIPG brainstem orthotopic xenograft mouse model (LI-F; H3WT subtype) using an alternative panobinostat dose schedule (10 mg/kg i.p., 5 d on, 5 d off). Mice treated with panobinostat on this regimen exhibited significantly prolonged survival compared to vehicle-treated controls (**Fig. 2i**, n = 10 per group, $P < 0.05$ by log-rank analysis).

Highlighting the need for effective combination therapies, DIPG cells that survived chronic panobinostat exposure demonstrated resistance when re-challenged with the drug (**Supplementary Fig. 10a**). A recent, elegant study demonstrated utility of the histone demethylase inhibitor GSK-J4 for treating DIPG[18]), so we tested GSK-J4 alone or in combination with panobinostat. Consistent with previous findings[18], GSK-J4 decreased cell viability in H3K27M DIPG cell cultures (**Supplementary Fig. 10b**). Panobinostat synergized with GSK-J4 in H3.3K27M mutant DIPG cells (**Supplementary Fig. 10c,d**). In contrast, panobinostat did not improve the efficacy of temozolomide, which demonstrated no evidence of cytotoxic activity against DIPG cells *in vivo* (**Supplementary Fig. 10e**).

The present study represents a collaborative effort to identify functionally relevant targets for therapy and develop an effective DIPG treatment strategy. Integration of genomic data and chemical screening data, validated by *in vivo* preclinical testing, converge to identify the potent HDAC inhibitor panobinostat as a promising therapy for DIPG. The finding that the leading DIPG therapeutic candidate is an epigenetic modifying agent is congruent with the discovery that the majority (~80%) of DIPG tumors harbor K27M mutations in the histone H3 genes *HIST1H3B* or *H3F3A* (refs. 4–6,19), which results in broad epigenetic dysregulation[7,8,16]. Indeed, epigenetic modifying therapies are emerging as the most promising class of agents for the treatment of DIPG[18]. The FDA-approved drug panobinostat could be rapidly translated for use in the clinic. Other classes of epigenetic modifying agents, such as histone demethylase inhibitors[18], may prove clinically useful for treating DIPG, alone or in combination, when such agents become available for clinical use.

Key caveats of our study should be noted: the drug screen used was not exhaustive, and future screening efforts may elucidate additional useful drugs. Further, *in vitro* systems do not model the cellular complexity of the tumor's microenvironment and thus do not screen for drugs that target key microenvironmental interactions. Nevertheless, by leveraging newly generated experimental model systems in an international collaborative effort, the data presented here define a promising therapy for a presently untreatable disease.

METHODS

Methods and any associated references are available in the online version of the paper.

Accession codes. Database of Genotypes and Phenotypes: Coordinates have been deposited with accession code phs000900.v1.p1 (RNA-seq and Whole Exome Sequencing data).

Note: Any Supplementary Information and Source Data files are available in the online version of the paper.

ACKNOWLEDGMENTS

We thank the many children and families who selflessly contributed to this study through tissue donations obtained from surgery or autopsy, and A. Gajjar for his guidance and vision throughout this study. We also thank D. Hargrave, J. Olson and S. Leary for selection of V.2 chemical screen agents. We are grateful for the critical questions and comments by S. Cheetham and N. Nsouli. We also acknowledge important comments by another DIPG Preclinical Consortium member, O. Becher. We thank G. Grant for assistance in developing rodent CED techniques. We thank R. Hashizume and C.D. James (Northwestern University) for use of the SF7761 DIPG cell line. Short-read sequencing was performed by the OHSU Massively Parallel Sequencing Shared Resource. This research is supported by the Lyla Nsouli Foundation, the Children's Oncology Group (COG) Central Nervous System Committee, the DIPG Collaborative (The Cure Starts Now Foundation, Reflections of Grace Foundation, Smiles for Sophie Foundation, Cancer-Free Kids Foundation, Carly's Crusade Foundation, Jeffrey Thomas Hayden Foundation, Soar with Grace Foundation), the Accelerate Brain Cancer Cures Foundation (ABC^2), CureSearch for Childhood Cancer, the Team Julian Foundation and the COG Chair's Grant (5UOCA098543). Additional funding support was provided by US National Institutes of Health grant K08NS070926 (to M.M.), Alex's Lemonade Stand Foundation (to M.M. and Y.T.), the McKenna Claire Foundation, the Connor Johnson Memorial Fund, the Dylan Jewett Memorial Fund, the Elizabeth Stein Memorial Fund, the Dylan Frick Memorial Fund, the Abigail Jensen Memorial Fund, the Zoey Ganesh Memorial Fund, the Wayland Villars DIPG Foundation, the Jennifer Kranz Memorial Fund, Unravel Pediatric Cancer, the Virginia & D.K. Ludwig Fund for Cancer Research, the Price Family Charitable Fund, the Matthew Larson Foundation, the Godfrey Family Fund in Memory of Fiona Penelope, the Child Health Research Institute at Stanford, the Anne T. and Robert M. Bass Endowed Faculty Scholarship in Pediatric Cancer and Blood Diseases (all to M.M.), Etoile de Martin (to J.G. and N.T.), Fondation Lemos and Le Défi de Fortunée (to J.G.), the Scott Carter Foundation (to N.E.B.), the Semmy Foundation (to D.G.v.V. and E.H.), the US Department of Defense (to X.-N.L.), National Science Foundation grant CCF0953366 (to R.P.), Marie Curie grant IRG270459 (to M.M.A.); the Spanish Ministry of Health grant PI13/0125 (to M.M.A.), and the St. Baldrick's Foundation and Iron Matt Foundation (both to E.R. and M.H.-C.).

AUTHOR CONTRIBUTIONS

C.K., M.M., J.G., Y.T., M.F., K.E.W., D.G.v.V., R.P., C.S.G., C.H., X.-N.L. and P.T.S. participated in the design or interpretation of the reported experiments or results. J.A., E.H., L.L., Y.T., A.P., S.C., P.J.W., T.B.J., M.H.-C., L.L.D., N.T., M.M., K.E.W., R.P., N.E.B., L.E.D., E.H.R. C.K., M.K., Y.D., L.Q., Y.H., C.S.G., M.Q., M.-A.D., J.N., M.M.A., W.S., E.C.H., M.J.Q., P.S.M., H.M., M.N.S., N.W. and X.-N.L. participated in the acquisition or analysis of data. M.M., C.S.G., C.K., J.G., Y.T., M.-A.D., L.L., R.P., N.T., E.H.R., D.G.v.V., N.E.B. and X.-N.L. participated in drafting or revising the manuscript. M.M., C.K., R.P. and J.G. supervised all aspects of the research.

COMPETING FINANCIAL INTERESTS

The authors declare competing financial interests: details are available in the online version of the paper.

Reprints and permissions information is available online at http://www.nature.com/reprints/index.html.

© 2015 Nature America, Inc. All rights reserved.

1. Donaldson, S.S., Laningham, F. & Fisher, P.G. *J. Clin. Oncol.* **24**, 1266–1272 (2006).
2. Monje, M. *et al. Proc. Natl. Acad. Sci. USA* **108**, 4453–4458 (2011).
3. Hashizume, R. *et al. J. Neurooncol.* **110**, 305–313 (2012).
4. Wu, G. *et al. Nat. Genet.* **44**, 251–253 (2012).
5. Schwartzentruber, J. *et al. Nature* **482**, 226–231 (2012).
6. Khuong-Quang, D.A. *et al. Acta Neuropathol.* **124**, 439–447 (2012).
7. Lewis, P.W. *et al. Science* **340**, 857–861 (2013).
8. Bender, S. *et al. Cancer Cell* **24**, 660–672 (2013).
9. Caretti, V. *et al. Acta Neuropathol.* **127**, 897–909 (2014).
10. Taylor, K.R. *et al. Nat. Genet.* **46**, 457–461 (2014).
11. Veringa, S.J. *et al. PLoS ONE* **8**, e61512 (2013).
12. Pal, R. & Berlow, N. In *Pacific Symposium on Biocomputing* 351–362 (2012).
13. Berlow, N. *et al. BMC Bioinformatics* **14**, 239 (2013).
14. Bradner, J.E. *et al. Nat. Chem. Biol.* **6**, 238–243 (2010).
15. Brown, Z.Z. *et al. J. Am. Chem. Soc.* **136**, 13498–13501 (2014).
16. Chan, K.M. *et al. Genes Dev.* **27**, 985–990 (2013).
17. Sandberg, D.I., Edgar, M.A. & Souweidane, M.M. *J. Neurosurg.* **96**, 885–891 (2002).
18. Hashizume, R. *et al. Nat. Med.* **20**, 1394–1396 (2014).
19. Sturm, D. *et al. Cancer Cell* **22**, 425–437 (2012).

© 2015 Nature America, Inc. All rights reserved.

ONLINE METHODS

Materials availability. All cell lines described here can be obtained through a Material Transfer Agreement with the originating institution (Stanford University, Johns Hopkins University, Gustave Roussy, Université Paris-Sud, VU Medical Center or Texas Children's Cancer Center).

Primary cell culture establishment and propagation. For all human tissue studies, informed consent was obtained and Institutional Review Board approval was granted at each participating institution. Cell culture models (SU, NEM, JHH, Li and VU cultures) were validated by DNA fingerprinting. SU, NEM and JHH lines were authenticated using short tandem repeat (STR) analysis (see **Supplementary Table 2**). Li cultures were authenticated using single-nucleotide polymorphism (SNP) analysis. VU lines were authenticated by routine Sanger sequencing for the K27M histone gene mutation. All cell cultures were routinely tested for mycoplasma. Please see **Supplementary Table 1** for age, sex and other clinical characteristics associated with each cell culture. Cultures were derived from the tumors of both male and female individuals aged 2–9 years.

Stanford cell lines (SU) and primary tumor cell culture. As previously described[2,9,10], tumor tissue was harvested under sterile conditions in the autopsy suite, collected in serum-free DMEM/12 (Cellgro) and transported on ice to the laboratory. The tissue was then minced with a sterile no. 10 scalpel and washed twice in HEPES-HBSS (HeHBSS) to remove debris. Minced tissue was then added to dissociation buffer (HeHBSS) with DNase I (250 U/ml) and collagenase type IV (1 mg/ml). Minimal mechanical force was used and the cells were allowed to dissociate at 37 °C on a nutator. The cells were then sequentially strained through a 100, 70 and 40 µM cell strainer, centrifuged and processed through a sucrose gradient. Dissociated cells were treated with ACK/RBC lysis buffer (0.15 M NH_4Cl, 1.0 mM $KHCO_3$ and 0.1 mM Na_2-EDTA) and plated in tumor stem media (TSM), which consisted of Neurobasal (−A) (Invitrogen, Carlsbad, CA), B27 (−A) (Invitrogen), human-bFGF (20 ng/ml) (Shenandoah Biotech, Warwick, PA), human-EGF (20 ng/ml) (Shenandoah), human PDGF-AB (20 ng/ml) (Shenandoah) and heparin (10 ng/ml). Cells were subsequently cultured as tumor neurospheres and passaged every 1–2 weeks.

Johns Hopkins cell line (JHH-DIPG-1). The JHH-DIPG-1 cell line was generated using the protocol described for the Stanford cell lines.

Gustave Roussy cell lines (NEM) and primary cell cultures. Tumor pieces were collected into DMEM (Dulbecco's Modified Eagles Medium, PAA Laboratories GmbH, Pasching, Austria). Biopsies were cut into 1 mm^3 pieces and placed either into DMEM for immediate processing or into freezing medium (90% serum, 10% DMSO) before being progressively cooled to −80 °C. Cell dissociation was performed mechanically by passage through increasingly finer needles (19–26 gauge (G)). Single cells were seeded in AmnioMAX C-100 complete medium containing gentamycin, L-glutamine and FBS (Gibco, Invitrogen, Paisley, UK) and maintained at 37 °C in a 5% CO_2, humidified atmosphere. The cells were further cultured until appearance of adherent cells and colony formation and then passaged weekly .

Texas Children's Hospital xenograft models and recovered cultures (Li). Tumor tissue was dissociated and immediately xenografted into the brains of NOD SCID mice (Jackson Laboratory). Tumors were passaged by serial xenografting and cell culture experiments were performed in recovered xenografts. The recovered xenograft cultures contain approximately 20% mouse cells and 80% human DIPG cells. Recovered xenograft cells were authenticated using single nucleotide polymorphism (SNP) analysis as described below.

The SF7761 DIPG cell line was cultured as previously described[3].

VU DIPG cell lines. VU-DIPG-A and VU-DIPG-B were cultured as previously described[11].

Chemical screens. A panel of 83 drugs (**Fig. 1a**) was developed for screening drug sensitivity of DIPG cells; the majority of these compounds are in clinical trials currently. Each compound was plated in four concentrations (10 µM, 1 µM, 100 nM and 10 nM) in triplicate in a 384-well format. Early passage cells cultured from autopsy or biopsy tissue were plated at a density of 2,500 cells/well and incubated at 37 °C with humidified 5% CO_2 for 3 d. Cell viability was determined by the CellTiter-Glo luminescent assay (cat #G7572, Promega, WI) per manufacturer's instructions and measured with the IVIS Lumina II imaging system. IC_{50} values were determined by a nonlinear best-fit method using Excel Solver (Microsoft Excel 2011).

DIPG orthotopic xenograft *in vivo* studies. All animal procedures were performed with approval from each institution's animal care and use committee (the Stanford University Administrative Panel on Laboratory Animal Care and the Baylor Institutional Animal Care and Use Committee) and adhered to the US National Institutes of Health guide for the care and use of laboratory animals. Both male and female animals were used equally.

Patient-derived H3K27M DIPG orthotopic xenograft model (Stanford University). DIPG pontine xenografts were generated as previously described[2]. Briefly, a single cell suspension was made of SU-DIPG-VI-luc neurospheres and 100,000 cells (50,000 cells/µl, 2 µl) were stereotactically injected into the fourth ventricle/pons of NOD SCID-IL2R-γ chain–deficient (NSG; Jackson Laboratory), cold-anesthetized, postnatal day 2 mouse pups by stereotactic injection through a 31G burr hole (stereotactic coordinates: 3 mm posterior to lambda suture and 3 mm deep.)

CED was performed 2 months post-xenograft using a 31G Hamilton with a 27G needle threaded on the outside in isoflurane-anesthetized animals[20]. (The inside needle is 1 mm longer than the outside needle in order to create the convection effects.) Infusion was performed using a digital pump set at a rate of 0.4 µl/min. Five microliters of 2 µM panobinostat (Selleck Chemicals) was delivered over a period of 12.5 min. Stereotactic coordinates (from surface of brain) used were from lambda AP −0.8 mm, lateral 1 mm and 5 mm deep. Controls received vehicle (DMSO diluted in 5% dextrose). *In vivo* bioluminescence imaging was performed before CED of panobinostat or vehicle, and again 7 d later, using an IVIS imaging system (Xenogen) under isoflurane anesthesia.

Systemic administration of panobinostat was performed with intraperitoneal injection 3 d per week (M, W, F) for dose levels 1 mg/kg and 10 mg/kg, and administered once per week for the 20 mg/kg cohort. Controls were injected i.p. with an identical volume of DMSO vehicle. Panobinostat was dissolved in 70 mg/ml DMSO, then serially diluted in water to a concentration of 0.1–2 mg/ml (depending on the target dose level) such that 10 µl/g or ~200 µl total was administered i.p. each dose.

For IVIS imaging analyses of *in vivo* DIPG tumor growth, animals were imaged at baseline. Animals were excluded if no tumors were present, and then animals were randomized to control and treatment groups such that each group had equivalent distribution of initial tumor sizes.

Patient-derived orthotopic xenograft model IBs-W0128DIPG (Texas Children's Hospital). This is a serial xenograft model. NOD SCID mice were implanted with 50,000 IBs-W0128DIPG cells (H3WT) into the brainstem ($n = 10$ per group) and treatment (panobinostat, 10 mg/kg, i.p.) was started 17 d after tumor implantation (5 d on, 5 d off, followed by another 4 d on) for a total of 9 doses.

Blinding was not performed.

LC-MS/MS analysis of panobinostat concentrations in tissues and serum. *Sample preparation*. A single 20 mg/kg dose was delivered i.p. in NOD-SCID-IL2R γ chain–deficient mice, and tissue samples collected 30 min later for analysis using liquid chromatography/tandem mass spectrometry (LC-MS/MS). Tissue samples were weighed and one volume of bullet blender beads (Next Advance) and two volumes of Milli-Q water were added. Tissues were homogenized by a bullet blender (Next Advance) at 4 °C according to manufacturer's instruction. Stock solution of neat panobinostat (Selleck Chemicals) and internal standard (IS) panobinostat-d8 (Toronto Research Chemicals, Canada) were prepared in methanol and further diluted in 50% methanol. For spiked standards, 25 µl of neat panobinostat (5 ng/ml–20 µg/ml) and 10 µl of IS (100 ng/ml) were added to 25 µl of blank tissue homogenate or serum. For samples, 25 µl of 50% methanol was used instead of neat panobinostat. 150 µl of methanol/acetonitrile 50:50 (v/v) was added to the mixture and vortexed vigorously for 1 min followed by centrifugation at 10,000 *g* for 5 min. For brain standards and samples, the supernatant was diluted three times with 0.1% formic acid (v/v) in water. For serum and kidney standards and samples, the supernatant was diluted 10 times and 100 times respectively, in 30% methanol with 0.1% formic acid.

LC-MS/MS analysis. The LC-MS/MS system consists of a QTRAP 4000 mass spectrometer (AB SCIEX) coupled to a Shimadzu UFLC system. LC separation was carried out on an ACE C18 column (50 mm × 2.1 mm, 5 µm) with isocratic elution using a mobile phase composed of 65% water and 35% methanol. 0.1% of formic acid was added to both aqueous and organic phases. The flow rate was set at 0.25 ml/min. Column temperature was 25 °C. The analysis time was

© 2015 Nature America, Inc. All rights reserved.

doi:10.1038/nm.3855

2.5 min. The injection volume was 10 µl. The mass spectrometer was operated in the positive mode with multiple-reaction monitoring (MRM). The *m*/*z* 350.2→158.1 and 358.3→164.2 transitions were used for panobinostat and panobinostat-d8 (IS). Data acquisition and analysis were performed using the Analyst 1.6.1 software (AB SCIEX).

Western blot analyses of protein levels and RT-qPCR analyses of RNA levels. For whole cell extract analyses, the cells were lysed by using RIPA buffer plus proteinase inhibitors. For chromatin extract analyses, chromatin extract was prepared as follows: cells were lysed in Buffer A′ (10 mM Tris-HCl, pH 7.5, 10 mM KCl, 1.5 mM $MgCl_2$, 0.34 M sucrose, 10% glycerol, 1 mM DTT, and protease inhibitors (1 mM phenylmethanesulfonylfluoride (PMSF) and 1× protease inhibitor cocktail from RIPA Lysis Buffer System; sc-24948, Santa Cruz Biotechnology)) with 0.2% Triton X-100 on ice for 10 min. Nuclei were pelleted by low speed centrifugation (5 min, 1,300 *g*, 4 °C) and then lysed in buffer B′ (3 mM EDTA, 0.2 mM EGTA, 1 mM DTT and protease inhibitors (see above)). Insoluble chromatin was collected by centrifugation (5 min, 1,700 *g*, 4 °C). The chromatin extract was prepared by MNase digestion in Buffer A′ with 2 mM $CaCl_2$ at 37 °C for 5 min. To stop the digestion, EDTA was added. NaCl and Triton X-100 were then added to concentrations of 150 mM and 0.5% respectively. Protein concentrations were measured by using Pierce BCA Protein Assay (Thermo Scientific) and equal amounts of cell extracts were loaded for western blot analysis. The primary antibodies used in this study were anti-mTOR (CST, #2972), anti-β-tubulin (Abcam, ab6046), anti-H3K27me3 (Abcam, ab6002), anti-H3Ac (H3-acetyl K9 + K14 + K18 + K23 + K27, Abcam, ab47915), anti-H3 (Abcam, ab1791), anti-HDAC1 (CST, #5356), anti-HDAC2 (CST, #5113), anti-EZH2 (Active motif, 39933) and anti-HA (Santa Cruz, sc-7392).

For RNA analyses, RNA extraction was performed by using Qiazol Lysis Reagent (79306, Qiagen, Venlo, Netherlands) according to the manufacturer's instructions. Reverse transcription was performed by using the High Capacity cDNA Reverse Transcription Kit (4368813, Invitrogen) and real-time qPCR was performed by using 2× Maxima SYBR Green qPCR Master Mix (#K0251, Thermo Scientific). qPCR primers are listed as follows: *CCND1*, 5′-TTCAAATGTGTGCAGAAGGA-3′ and 5′-GGGATGGTCTCCTTCATCTT-3′; *MKI67*, 5′-TTGGAGAATGACTCGTGAGC-3′ and 5′-CGAAGCTTTCAATG ACAGGA-3′; *HDAC1*, 5′-ATCGGTTAGGTTGCTTCA-3′ and 5′-TCATTCG TGTTCTGGTTAGTC-3′; *HDAC2*, 5′-GACAGTGGAGATGAAGATGGA-3′ and 5′-TTCTGATTTGGTTCCTTTGG-3′; *GAPDH*, 5′-TGACTTCAACAGC GACACCCA-3′ and 5′-CACCCTGTTGCTGTAGCCAAA-3′.

Cell viability, cellular proliferation and apoptosis analyses. GSK-J4, BEZ235, AUY922, carfilzomib, panobinostat, vorinostat, flavopiridol, BKM120, AZD8055, RAD001 and temozolomide were purchased from Selleck Chemicals (Houston, TX, USA). For generating drug dosage curves or time-course growth curves, cells were plated at a density of 5,000 cells/well in 96-well plates in at least triplicate and then subjected to drug treatment for 72 h as indicated. Cell viability was then measured using CellTiter-Glo assay according to the manufacturer's instructions (G7571, Promega, WI, USA), and data were collected on a TECAN Infinite 200 plate reader. For testing combinatory effects of two drugs, the cells were treated with each drug individually or in combination before subjecting to CellTiter-Glo assay. CalcuSyn software (Biosoft, Cambridge, UK) was used to calculate the combinatory index (CI). CI less than 1.0 was considered to be synergistic.

Cellular proliferation was measured by using the Click-iT EdU Alexa Fluor 488 Flow Cytometry Assay Kit according to the manufacturer's instructions (C35002, Invitrogen, CA, USA). The EdU^+ population represented the proliferating cell population. DIPG cells were treated with 0.1% DMSO vehicle or panobinostat at 0.1 or 0.5 µM respectively for 24 h and then incubated with 10 µM EdU for another 16 h. Cells were then subjected to EdU FACS analysis to assess the proportion of cells in S-phase (EdU^+). Cellular apoptosis was measured by using Annexin V-FITC Apoptosis Detection Kit II (556570, BD Biosciences, CA, USA) with some minor modifications. DAPI was used in the staining instead of PI. DIPG cells were treated with 0.1% DMSO or panobinostat at 0.1 or 0.5 µM for 48 h and then subjected to Annexin V/DAPI FACS analysis to assess the proportion of cells undergoing apoptosis. For FACS analyses, the stained cells were analyzed using BD Fortessa FACS machine (BD Biosciences). The data were analyzed using FlowJo software (FlowJo, LLC).

shRNA-expressing lentivirus preparation and infection. shRNA expressing lentiviral constructs against human *mTOR*, *HDAC1* and *HDAC2* from the RNAi consortium human collection were purchased from Sigma. Lentiviral expressing constructs were co-transfected with packaging plasmids (pDelta 8.92 + VSV-G) into 293T cells to generate lentiviral particles. Lentiviral particles were then concentrated by polyethylene glycol (PEG) precipitation method. The precipitated lentiviruses were resuspended in PBS and aliquoted for −80 °C storage. For lentiviral infection, DIPG cells were incubated with shRNA expressing lentivirus for 16 h. 48 h after infection, puromycin (0.5 µg/ml) was added to select virally infected cells for further experiments. Cells were seeded in triplicate into 96-well plates and cell viability was assessed using the CellTiter-Glo assay at 0, 3 and 5 d.

Testing for resistance to panobinostat in DIPG cell cultures. SU-DIPG-VI and SU-DIPG-XIII cells were exposed to panobinostat at ~IC_{50} dose (0.05 µM for SU-DIPG-VI and 0.1 µM for SU-DIPG-XIII) chronically for 3 weeks. The old culturing medium was replaced with fresh drug-containing medium every 3–4 d.

DNA and RNA sequencing. For all human tissue studies, informed consent was obtained and institutional review board approval was granted at each participating institution. Please see **Supplementary Table 1** for age, sex and other clinical characteristics associated with each cell culture. Age range, 2–21 years and approximately equal distribution of male and female individuals.

Generation of exome-capture libraries. Exome libraries of matched pairs of tumor/normal genomic DNAs were generated using the Agilent SureSelect XT kit and Agilent Automation Systems NGS system per manufacturer's instructions. 1 µg of each genomic DNA was sheared using a Covaris E220 to a peak target size of 150 bp. Fragmented DNA was concentrated using AMPure XP beads (Beckman Coulter), and DNA ends were repaired using T4 DNA polymerase, Klenow polymerase and T4 polynucleotide kinase. 3′ A-tailing with exo-minus Klenow polymerase was followed by ligation of Agilent paired-end oligo adaptors to the genomic DNA fragment. Ligated DNA was PCR amplified for eight cycles and purified using AMPure XP beads and quantitated using the Quant-It BR kit (Invitrogen). 500 ng of sample libraries were hybridized to the Agilent biotinylated SureSelect v4 Exome + UTR Capture Library at 65 °C for 72 h following the manufacturer's protocol. The targeted exon fragments were captured on Dynabeads MyOne Streptavidin T1 (Invitrogen), washed, eluted, and enriched by amplification with Agilent post-capture primer and an indexed reverse primer for multiplexing 12 additional cycles. After purification of the PCR products with AMPure XP beads, the quality and quantity of the resulting exome libraries were analyzed using an Agilent Bioanalyzer High Sensitivity chip.

Somatic point mutation identification by exome capture sequencing. The methodology described below is a minor modification of the approach described in ref. 21. All captured DNA libraries were sequenced with the Illumina HiSeq in paired-end mode, yielding 80 base pairs from the final library fragments. The reads that passed the chastity filter of Illumina BaseCall software were used for subsequent analysis. Mate pairs were pooled and mapped as single reads to the reference human genome (NCBI build 36.1, hg18), excluding unordered sequence and alternate haplotypes, using Bowtie[22] keeping unique best hits, and allowing up to two mismatched bases per read. Likely PCR duplicates, defined as reads with equal match intervals on the reference genome, were removed; and individual basecalls with Phred quality less than Q20 were excluded. A mismatched base (SNV) was identified as a variant when (i) it had at least six reads of support, (ii) it constituted at least 10% of the coverage at that position, (iii) it was observed on both strands and (iv) it fell within 50 bases of a region targeted for capture.

In matched samples (samples with matched normals), a variant was called somatic if (i) there was 8× coverage in the matched normal, (ii) it did not occur in the matched normal sample in more than two reads and 2% of the coverage (or 4% of the coverage if the tumor variant fraction was at least 20%), (iii) if it had any support in the matched normal and (iv) it was not present in either dbSNP (v137) or the Exome Sequencing Project data set (ESP6500).

In unmatched samples, a variant was called probable somatic if it affected the same codon as either a somatic point mutation observed in the matched samples or a somatic mutation from COSMIC (v66).

© 2015 Nature America, Inc. All rights reserved.

Finally, all somatic/probable somatic variants were screened against the full set of benign samples. Variants were removed from further consideration if they appeared in any benign sample with at least three reads and 10% of the coverage.

Identification of coding indels in exome capture data. The methodology for identifying indels in exome capture data was adapted from ref. 23 with minor modifications. Reads for which Bowtie was unsuccessful in identifying an ungapped alignment were converted to FASTA format and mapped to the target regions, padded by 200 bases on either side, with cross_match (v0.990329, http://www.phrap.org), using parameters –gap_ext -1 –bandwidth 10 –minmatch 20 –maxmatch 24. Output options were –tags –discrep_lists –alignments. Alignments with an indel were then filtered for those that: (i) had a score at least 40 more than the next best alignment, (ii) mapped at least 75 bases of the read, and (iii) had two or fewer substitutions in addition to the indel. Reads from filtered alignments that mapped to the negative strand were then reverse-complemented and, together with the rest of the filtered reads, remapped with cross-match using the same parameters (to reduce ambiguity in called indel positions due to different read orientations). After the second mapping, alignments were re-filtered using the same criteria as for initial filtering. Reads that had redundant start sites were removed as likely PCR duplicates, after which the number of reads mapping to either the reference or the non-reference allele was counted for each. An indel was identified as a variant when (i) it had at least six reads of support, (ii) it constituted at least 10% of the coverage at that position, (iii) it was observed on both strands and (iv) it fell within 50 bases of a region targeted for capture. Indels were reported with respect to genomic coordinates. For insertions, the position reported is the last base before the insertion. For deletions, the position reported is the first deleted base.

In matched samples, an indel was called somatic if there was 8× coverage in the matched normal, if it had any support in the matched normal, and it was not present in either dbSNP (v137) or the Exome Sequencing Project data set (ESP6500). In both matched and unmatched samples, all remaining indels were screened against the full set of benign samples. Variants were removed from further consideration if they appeared in any benign sample with at least three reads. **Supplementary Table 3** provides the somatic point mutation and indels called in matched and unmatched samples in drug target genes as well as the somatic point mutations and indels called using matched samples.

Annotation. We annotated the resulting somatic mutations using CCDS transcripts wherever possible. If no CCDS transcript was available, we use the coding regions of RefSeq transcripts. HUGO gene names were used.

Exome copy number analysis. Copy number aberrations were quantified and reported for each gene as the segmented normalized $\log_2$-transformed exon coverage ratios between each tumor sample and its matched normal as described in ref. 24. For unmatched samples, we used the average coverage derived from the full set of benign samples as a 'normal pool;' for chromosomes X and Y only, we formed separate normal pools from the XX and XY benign samples. We identified segments as focal if they contained 10 or fewer CCDS gene annotations. To identify a gene as gained or lost we first considered the segmented data, requiring a copy number gain or loss of 30% (ratio > = 1.3 or < = 0.7) to call the gene as gained or lost. In addition, we considered the distribution of copy number estimates for each gene's individual exons. If the mean exonic copy number showed a gain or loss of at least 30% and deviated from the null hypothesis by at least 2.5 s.d., we called the gene gained or lost.

For the total copy-number call over all tumor tissue samples, we counted each gain or loss of at least 60% as ± 2 on its respective segment, and each gain or loss of 30–60% as ± 1, and summed these contributions across all tumor tissue samples. In order to omit germline CNVs from the total, we looked at segmented exon coverage ratios between the individual normal samples and the normal pool. Any segment that was gained or lost by 30% in at least two normal samples was flagged as a probable CNV, and was not included in the total copy-number sum.

Generation of RNA-seq libraries. RNA-seq libraries for transcriptome analysis were prepared using the TruSeq RNA Sample Preparation Kit (Illumina) and Agilent Automation NGS system per manufacturers' instructions. Sample prep began with 1 μg of total RNA from each sample. Poly-A RNA was purified from the sample with oligo dT magnetic beads and fragmented with divalent cations. Fragmented poly-A RNA was converted into cDNA through reverse transcription and was repaired using T4 DNA polymerase, Klenow polymerase, and T4 polynucleotide kinase. 3′ A-tailing with exo-minus Klenow polymerase was followed by ligation of Illumina paired-end oligo adapters to the cDNA fragment. Ligated DNA was PCR amplified for 15 cycles and purified using AMPure XP beads. After purification of the PCR products with AMPure XP beads, the quality and quantity of the resulting transcriptome libraries were analyzed using an Agilent Bioanalyzer High Sensitivity chip.

Gene expression in RPKM inferred from RNA-seq data. All transcriptome libraries were sequenced with the Illumina HiSeq in paired end mode. The reads that passed the chastity filter of Illumina BaseCall software were used for subsequent analysis. We trimmed all reads to 85-mers and aligned them to the reference human genome (NCBI build 36.1, hg18), plus a splice junction set including 84 bases on either side of the 2008 Illumina splice junction set, using Bowtie[22] in single read mode, keeping unique best hits and allowing up to two mismatched bases. Mate pairs from paired-end runs were pooled and treated as single reads.

Next, all of the exons for a single gene were concatenated to form a single 'transcript' for that gene. Reads that mapped to the exons in the gene, as well as reads that mapped to the splice junctions, were remapped to the transcript. We then walked the transcript and summed the coverage at each position, then divided the result by the transcript length × the number of reads in the sample, and then multiplied the result by one million. This method is a modified version of the one described in ref. 25.

DNA fingerprinting using common high-frequency variants. We considered 147 genomic positions that tended to have good coverage in both whole-exome and RNA-seq data and for which at least two alleles were widespread. For each sample, we constructed a 'fingerprint' for those positions with at least six fragments of coverage; an allele was included in the fingerprint if it was seen in at least two fragments of coverage and at least 15% of the total fragments. Two samples were deemed a match if at least 85% of the positions with sufficient coverage in both samples had identical fingerprints. In practice, samples from the same patient matched at 90% of positions, whereas samples from different patients matched at 75% of positions. For this study, all the included samples from the same patient met the 85% match criteria, including all RNA-seq and exome samples. In addition, no samples from different patients exceeded 74% similarity.

RNA-seq of panobinostat-treated cultures. RNA-seq was performed as above in SU-DIPG-IV and SU-DIPG-VI cell lines following exposure to 1 μM panobinostat (Selleck Chemicals) for 48 h. RNA-seq was also performed in SU-DIPG-IV, SU-DIPG-VI and JHH-DIPG1 cell lines following exposure to 0.1 μM panobinostat (Selleck Chemicals) for 24 h in triplicate. Cells were then lysed and RNA extracted in TRIzol solution.

Post-panobinostat RNA-seq data analysis. There was a good concordance for the ratio of panobinostat-treated to vehicle-treated cell gene expression and the distribution of RPKM values were similar between cell lines and with the two conditions. In general, the variability in terms of ratio was low, usually below 1.

Gene set enrichment analysis. RNAseq profiles were preprocessed by applying the following filters: minimum RPKM ≥ 0.5 and maximum RPKM ≥ 10. Gene set enrichment analysis (GSEA) was then performed as previously described (http://www.broadinstitute.org/gsea/index.jsp). MSigDB-C2 (curated gene sets) and MSigDB-C5 (GO gene sets) databases were applied to gene set size filters (min, 15; max, 500). After that, 2,557 gene sets from the MSigDB-C2 database and 586 gene sets from the MSigDB-C5 database were used in GSEA. Five additional H3.3K27M-related gene sets were also used. The five H3.3K27M-related gene sets were CHAN_NSC_ONLY (genes with H3K27me3 peaks only in NSC line but not in SF7761 H3.3K27M DIPG line), CHAN_SF7761_ONLY (genes with H3K27me3 peaks only in SF7761 H3.3K27M DIPG line but not in NSC line), CHAN_NSC SF7761_OVERLAP (genes with overlapping H3K27me3 peaks in NSC line and SF7761 H3.3K27M DIPG line), BENDER_K27M_UP (significantly upregulated genes in K27M pHGG tumors compared to WT pHGG tumors, defined as fold change ≥2, $P < 0.01$; Student's *t*-test, Benjamini–Hochberg correction) and BENDER_K27_DOWN (significantly downregulated genes in K27M pHGG tumors compared to WT pHGG tumors, defined as fold change

© 2015 Nature America, Inc. All rights reserved.

doi:10.1038/nm.3855

≤0.5, $P < 0.01$; Student's *t*-test, Benjamini–Hochberg correction). Enriched gene sets were selected using a cut-off of FDR ≤ 0.1. Then, Venn diagram analysis was used to identify the shared enriched gene sets of the four RNA-seq data sets (SU-DIPG-IV-DMSO or Pano 0.1 μM, SU-DIPG-VI-DMSO or Pano 0.1 μM, SU-DIPG-IV/IV-DMSO or Pano 1 μM and JHH-DIPG1-DMSO or Pano 0.1 μM).

Predictive analysis to identify relevant targets for therapeutic intervention. In this section, we discuss methodology and present results for a computational model of drug sensitivity designed to identify relevant functional targets in DIPG. We used the Target Inhibition Map (TIM) approach[12,13] to generate multivariate blocks of targets whose joint inhibition is predicted to increase drug sensitivity. This approach incorporates only functional drug screen–sensitivity values with available RNA-seq expression data to identify key functional targets in the disease cohort.

Data pre-processing and notations. For this analysis, we considered a total of six samples that had both drug sensitivity and RNA expression data. A subset consisting of eight cell lines was tested on drug screen 1 (SU-DIPG-IV, SU-DIPG-VI, VU-DIPG.A, NEM-145, NEM157) and another subset of seven cell lines was tested on drug screen 2 (NEM-163, NEM-165, NEM-168, NEM-175, JHH-DIPG1, NEM-157, NEM-215), with two cell lines tested on both screens.

To identify the mechanistic targets through which drugs derive their sensitivity, prior information on the kinase targets of the compounds is used. The drug target–inhibition information is contained in a matrix Δ which quantifies the ability of a drug to inhibit its kinase targets. Each row vector is relatively sparse, as most drugs inhibit a select few primary targets and a small set of secondary, but often relevant, side targets. Each entry of Δ is a real number between 0 and 1 denoting the inhibition of the kinase target. An entry of Δ is close to 1 when a small concentration of a drug can phosphorylate 50% of the kinase target. The matrix Δ is generated based on published drug target K_d's or EC_{50}'s from http://pubchem.ncbi.nlm.nih.gov/ and related publications. We used a Hill curve interpolation with Hill coefficient of 1 and a drug concentration of 10,000 nM to convert the EC_{50}'s to normalized inhibitions between 0 and 1. For each drug tested over a cell line, the functional response is measured as cell viability (the percentage of living cancerous cells following 72 h application of a drug). The cellular death rate for each drug, considered as the percentage of cancerous cells killed following 72 h application of the drug, is simply 1 – cell viability. The cellular death rate values are tested with three replicates in four concentrations. The cellular death rate values are converted to IC_{50}'s via Hill curve interpolation. The IC_{50} values are then converted to sensitivities between 0 and 1 using a Hill curve with a Hill coefficient of 1 and drug concentration of 10,000 nM. A NaN or NA IC_{50} is converted to sensitivity 0. This set of sensitivities is a matrix denoted by Σ. Note that we have a matrix Σ of size 60 × 8 for drug screen 1 and a matrix Σ of size 60 × 7 for drug screen 2.

To incorporate the mutation characterization, we considered the set of kinase targets present in the drug screen (denoted by Θ_1) and created a binary matrix M_0 which denotes whether each of the drug targets is mutated or not for each cell line. Considering the common 404 targets of the two drug screens, the size of M_0 is 15 × 404 where 15 denotes the cell lines (two rows are repeated as there are 10 unique cell lines).

To incorporate RNA expression data generated from the RNA-seq experiments, we consider the set of kinase targets present in the drug screen (Θ_1) and the targets with quantified expression present in the RNA-seq data (Θ_2). The set of targets for which we have usable information is then $\Theta_1 \cap \Theta_2$, the intersection of the two target sets. The remaining targets in Θ_1 are targets for which we do not have any RNA expression information and thus we are only able to gain information on these kinase targets from the drug screen data. Let the RNA expression be given by matrix G_0. In this analysis, the set $\Theta_1 \cap \Theta_2$ has 403 targets and thus the size of G_0 is 15 × 403. The RNA expression matrix is converted to a normalized matrix G by dividing the RNA expression of each gene by the mean expression of the matched normal samples or mean expression values. Thus, a value >>1 in G denotes that the gene is highly expressed for that sample compared to normal matched samples or the expression mean.

TIM predictive algorithm to identify multivariate target combinations for therapeutic intervention. In this section, we utilize the target inhibition map approach for target selection and sensitivity prediction. We next provide a brief outline of the approach (for details, please refer to ref. 13).

The primary goal of the TIM model is to generate hypotheses of sets of targets that can potentially produce desirable treatment results based on the available drug screen and gene expression data.

There are two main steps in the TIM method. Step one is selection of the optimal drug targets based on functional data generated from drug screens. This is the model-generation step in the TIM algorithm. The model generation is approached from a Boolean logic perspective, where we aim to generate logical relationships between targets that identify the mechanisms by which tumors persist. Because of the Boolean nature of the approach, the matrix Δ generated for this analysis consists of 0's or 1's. The drug inhibition profiles (in the form of target EC_{50}'s) are used to generate the binarized inhibition vectors based on the drug's IC_{50} value. The binarized vectors are generated based on the following equation:

$$a\log(\mathrm{IC}_{50}) \le \log(\mathrm{EC}_{50}) \le b\log(\mathrm{IC}_{50}), 0 \le a << b$$

This binarization approach uses the functional drug sensitivity data to generate vectors of relevant drug targets. We assume that any target sufficiently beyond the IC_{50} point is unlikely to have been the cause of the drug response, and thus we assume that we cannot gain information from it.

To generate drug sensitivity values from the IC_{50} response data, we use the following equation:

$$y_i = \frac{\log(MaxDose_i) - \log(\mathrm{IC}_{50,i})}{\log(MaxDose_i)}$$

where $IC_{50,i}$ is the $IC_{50,i}$ of drug *i*, $MaxDose_i$ is the maximum tested dosage of drug *i* and y_i is the resulting sensitivity value of drug *i*.

To incorporate RNA-seq data into the TIM analysis, we eliminate unlikely kinase targets from consideration based on G, the matrix of normalized RNA expressions over the set $\Theta_1 \cap \Theta_2$. A kinase target is kept in the data set for consideration if $G_{(i,j)} > \rho$, a threshold for minimum relative expression. Note that we are considering expressed targets only, as the effect of a molecularly targeted drug is to inhibit the target when it is expressed, and thus non-expressed drug targets will have limited effect on predicting the drug response. For the purpose of this project, the RNA expressions constraint was $G_{(i,j)} > \rho = 1$, meaning the RNA expression of the cancerous line must be at least that of the matched normal expression. As G does not provide information about the remaining targets in $\Theta_1 - \Theta_2$, they are not eliminated from consideration as they could potentially be driver mechanisms for the tumor. We performed the primary analysis on the 16 sets of joint RNA-seq-matched and cell line drug screen data.

Subset-superset biological constraint. We utilize the following biological constraints to identify consistent and inconsistent sets of protein targets[13]:

For any drug d_1 and any kinase target set S_T,

Constraint 1: if $\Delta(d_1, S_T) \preccurlyeq \Delta(d_2, S_T)$, then $\Sigma(i, d_1) \le \Sigma(i, d_2)$ (more inhibition of oncogenes will improve sensitivity).

Constraint 2: if $\Delta(d_1, S_T) \succcurlyeq \Delta(d_2, S_T)$, then $\Sigma(i, d_1) \ge \Sigma(i, d_2)$ (less inhibition of oncogenes will reduce sensitivity).

Here, the $\preccurlyeq$ and $\succcurlyeq$ operators signify component-wise inequality in all components.

The vectors and associated sensitivity values from matrix Σ are used to select the optimal targets for the TIM model. The optimal targets are selected by solving the following optimization problem that incorporates the inter-bin error (the error associated with multiple drugs having the same inhibition profile but differences in their sensitivity values) and the inconsistency error (the error associated with drug A being less effective than drug B but the targets of drug B are a subset of drug A's targets). In this context, a bin is any subset of a set of kinase targets selected to build the model. The equation for inter-bin error is given by $\Sigma_{bins} \Sigma_{j \in bin} |P(s_j|T) - Y(s_j|T)|$, where $P(\bullet)$ is expected sensitivity of s_j under target set *T*, and $Y(\bullet)$ is the experimental sensitivity of s_j under target set *T*. The inter-bin error amounts to ensuring that kinase inhibitors with similar inhibition profiles with respect to the model have similar experimental sensitivities, indicating the likely mechanisms have been identified. The inconsistency error incorporates the subset-superset biological constraint introduced previously and

© 2015 Nature America, Inc. All rights reserved.

is given by the following equation: $\Sigma_{drugs}\Sigma_{bins}\chi(bin,drug)|P(s_j|T) - Y(s_j|T)|$, where $P(\bullet)$ and $Y(\bullet)$ are as above and $\chi(\bullet)$ is an indicator function which is 1 when the subset-superset constraint is violated. The total optimization problem we wish to solve then is

$$\sum_{bins}\sum_{j\in bin}|P(s_j|T)-Y(s_j|T)|+\sum_{drugs}\sum_{bins}\chi(bin,drug)|P(s_j|T)-Y(s_j|T)|.$$

We find the minimum solution to the optimization problem using a suboptimal search algorithm known as sequential floating forward search (SFFS). The TIM framework requires that the subset-superset biological constraints are satisfied during model generation. This allows for identification of unique target combinations that may not be identified as relevant through a standard linear modeling approach.

Step two in TIM analysis is sensitivity prediction based on selected targets from step one. This step is used to generate the TIM circuit, which provides a visual representation of effective treatments inferred from the functional data. To generate the target blocks, viable target combinations are explored systematically in a breadth-first search style approach. Here, desired sensitivity levels for each level of inhibition (in terms of targets inhibited) is specified by the user; based on this specification, combinations of targets that satisfy the desired sensitivity levels are selected and no further supersets of the combination are considered. The inferential steps are based on bounding the expected sensitivity by the closest subset of the target combination and the closest superset of the target combination. The equation for inferred sensitivity for a target set $\{t_1,t,t_2,\ldots t_n\}$ is given by

$$y(\{t_1,t_2\ldots,t_n\}) = y_l + (y_u - y_l)\left(\frac{\Sigma_{i=1}^{n}\alpha(t_i)}{\Sigma_{i=1}^{h}\alpha(t_i)}\right)^{\beta},$$

where y_l is the maximum sensitivity of the subsets of $\{t_1,t,t_2,\ldots t_n\}$, y_u is the minimum sensitivity of the supersets of $\{t_1,t,t_2,\ldots t_n\}$, $\alpha(\bullet)$ is weight for a kinase target, and β determines the order of the curve fit for $y(\{t_1, t_2,\ldots, t_n\})$. For this analysis, $\alpha(\bullet) = 1$ for all targets meaning all targets have equal weight and $\beta = 1$ which provides a linear fit. The sum in the denominator is the sum of weights between the subset generating y_l and the superset generating y_u. In this way, the predicted sensitivity lies between y_l and y_u depending on the distance of $\{t_1, t_2,\ldots, t_n\}$ to the subset and superset. Based on the number of additional targets needed to move from the subset to the desired target combination, the sensitivity of the drug combination is inferred. In the event, the predicted sensitivity $y(\{t_1, t_2,\ldots, t_n\})$ is sufficient to satisfy the sensitivity level defined by the user, the target combination is designated a valid block combination, and the supersets are no longer considered.

In **Supplementary Figure 3b** is the TIM model generated for the set of available DIPG drug screen data. Note that TIM analysis generates potential targets from drug screen information and uses the gene expression to remove false positives. Since the drugs considered inhibit oncogenes, we keep the targets that are differentially expressed in tumor cell lines as compared to normal cell lines. If a TIM analysis target is differentially expressed in at least one tumor cell line, the target is considered relevant. The number of genes displayed in **Supplementary Figure 3b** belongs to blocks whose scores[13] are above a threshold of 0.5.

Supplementary Figure 4 contains the results of *in vitro* drug combination testing and synergy analysis for a target combination predicted by the TIM modeling approach to have *in vitro* synergy.

The Chou–Talalay combination index (CI) was used to detect synergy (CI < 1). The CI is calculated based on the following equation:

$$\mathrm{CI} = \frac{D_1}{D_{x1}} + \frac{D_2}{D_{x2}}$$

where D_1 and D_2 denotes the combination dosages tested for drugs 1 and 2 to achieve δ% inhibition and D_{x1} and D_{x2} denote the corresponding dosages of individuals drugs 1 and 2 required to inhibit δ%.

To provide quantification for the predictive power of the TIM approach, 10-fold cross validation mean absolute errors (MAE) and correlation coefficients between experimental and predictive sensitivities were calculated. The first test used only the functional data generated from the Drug Screens for prediction. For this analysis the 10-fold CV error was 0.101 with a correlation coefficient of 0.848. The second test incorporated the RNA expression data to eliminate potential false positives before model development. Here the 10-fold CV error was 0.111 with a correlation coefficient of 0.773.

Statistical analyses. Bioinformatic and computational methods are described above. IC_{50} values were determined by a nonlinear best-fit method using Excel Solver. For comparison of gene expression levels of the 429 genes associated with the targets of the drug screen, we generated RNA-seq data and then compared tumor tissues to normal tissues to generate significance scores using a *t*-test with the Benjamini–Hochberg multiple comparison correction.

Sample size for *in vivo* experiments was based on variance estimated from pilot experiments with control pontine DIPG xenograft animals showing a s.d. of approximately 30% of the mean. Sample size calculations to detect a 50% difference in tumor growth between two groups with an alpha of 0.05 and power 0.8 indicated a minimum group size of three animals.

Two-tailed *t*-tests and two-way ANOVAs were used for *in vitro* experiments. A two-tailed *t*-test was used for comparison of tumor growth rate in treatment groups in orthotopic xenograft experiments; a log-rank test was used for orthotopic xenograft survival analysis.

Outlying data points (>2 s.d. from the mean in either direction) were excluded. Variance was similar between groups compared.

20. Sewing, A.C. *et al. J. Neurosci. Methods* **238**, 88–94 (2014).
21. Grasso, C.S. *et al. Nature* **487**, 239–243 (2012).
22. Langmead, B., Trapnell, C., Pop, M. & Salzberg, S.L. *Genome Biol.* **10**, R25 (2009).
23. Ng, S.B. *et al. Nature* **461**, 272–276 (2009).
24. Lonigro, R.J. *et al. Neoplasia* **13**, 1019–1025 (2011).
25. Mortazavi, A., Williams, B.A., McCue, K., Schaeffer, L. & Wold, B. *Nat. Methods* **5**, 621–628 (2008).

© 2015 Nature America, Inc. All rights reserved.

doi:10.1038/nm.3855